Acoustically induced cavity cloud generated by air-gun arrays—Comparing video recordings and acoustic data to modeling

Babak Khodabandeloo, and Martin Landrø

Citation: The Journal of the Acoustical Society of America **143**, 3383 (2018); doi: 10.1121/1.5040490
View online: https://doi.org/10.1121/1.5040490
View Table of Contents: http://asa.scitation.org/toc/jas/143/6
Published by the Acoustical Society of America

Acoustically induced cavity cloud generated by air-gun arrays—Comparing video recordings and acoustic data to modeling

Babak Khodabandeloo[a)]
Department of Geoscience and Petroleum, Norwegian University of Science and Technology (NTNU), NO-7491 Trondheim, Norway

Martin Landrø
Department of Electronic Systems, Norwegian University of Science and Technology (NTNU), NO-7491 Trondheim, Norway

(Received 22 November 2017; revised 16 May 2018; accepted 16 May 2018; published online 7 June 2018)

For seismic air-gun arrays, ghost cavitation is assumed to be one of the main mechanisms for high-frequency signal generation. Ghost cavitation signals are weak for seismic frequencies (<300 Hz) and do not contribute to seismic reflection profiling. In the current experiment, the ghost cavity cloud is monitored by a high-speed video camera using 120 frames per second. This is, as far as the authors know, the first convincing photographic evidence of ghost-induced cavitation. In addition to video recording, acoustic signals were recorded with a sampling rate of 312.5 kHz using broadband hydrophones suspended 17 m below the array. The pressure drop around the source array is estimated using air-gun modeling followed by a phenomenological modeling of the growth and collapse of each vapor cavity. The cumulative effect of cavity collapses is modeled based on linear superposition of the acoustic signals generated by individual cavities. The simulated acoustic ghost cavitation signal and the corresponding cavity cloud show good agreement with the field data.
 https://doi.org/10.1121/1.5040490

[BTH] Pages: 3383–3393

I. INTRODUCTION

In marine seismic reflection profiling where the geological structure beneath the seabed is delineated, marine seismic sources such as air-guns, water-guns, and marine vibrators are used (Duren, 1988). The objective of such exploration surveys is usually to find hydrocarbon resources. Other applications are academic research and mapping of Earth's subsurface. By far, air-gun arrays have been the most prevalent and efficient marine seismic source (Duren, 1988; Barger and Hamblen, 1980) and still are (Watson *et al.*, 2016). An air-gun generates acoustic pressure waves from expansion and contraction of an air bubble which is formed by releasing high-pressure air (typically 2000 psi) into the surrounding water within a short time (Caldwell and Dragoset, 2000). Instead of using a single air-gun, several air-guns with different air chamber volumes are arranged in arrays and fired simultaneously to produce and direct an intense pulse towards the seabed (Dragoset, 2000).

It is the low-frequency band (<300 Hz) that is analyzed in seismic reflection profiling (Caldwell and Dragoset, 2000) and hence ideal air-gun arrays should produce acoustic pressure waves containing all energy concentrated below 300 Hz. However, measurements with broadband hydrophones have revealed that the acoustic signal from air-gun arrays contains frequencies up to tens of kHz (Goold and Fish, 1998; Tashmukhambetov *et al.*, 2008; Landrø *et al.*, 2011; Guan *et al.*, 2015). Such high frequencies are much weaker than the low-frequency parts and do not benefit seismic imaging, but they can be used, for example, to detect targets of size between 0.5 and 20 m in the water column (Banda and Blondel, 2016) or for detection of potential gas leakage from an oil and gas production field or a CO_2 storage site (Landrø *et al.*, 2017). These high frequencies might impact cetacean species that are sensitive to acoustic signals in the high-frequency range (10–150 kHz) (Ketten, 2004; Landrø *et al.*, 2011).

Several mechanisms are responsible for high-frequency acoustic wave generation by air-gun arrays. The rapid movement of air from the air-gun into the water generates some amount of high frequencies. To reduce these high frequencies, a new air-gun has been designed and tested (Coste *et al.*, 2014; Gerez *et al.*, 2015) which releases the pressure over a longer time period compared to standard air-guns and hence the signature has a gentler slope and the peak amplitude is reduced (Groenaas *et al.*, 2016). To reduce the high-frequency generation due to the steep rise time of pressure, another solution is to use sources with lower operating pressures and larger volumes (Chelminski, 2015). For example, the tuned pulse source has a large air chamber filled with low-pressure air and generates acoustic pulses with long rise times (Ronen and Chelminski, 2017). King *et al.* (2015) and King (2015) suggest that the reflected ghost pressure wave from the sea surface interacts with the air-gun bubble and give rise to high frequencies between 400 to 600 Hz.

Another mechanism related to air-gun arrays, which generates high frequencies up to tens of kHz, is the ghost cavitation phenomena (Landrø *et al.*, 2011). Landrø *et al.* suggest that a cavity cloud is formed by the hydrostatic

[a)]Electronic mail: babak.khodabandeloo@ntnu.no

pressure drop in some locations around the array: acoustic pressures from individual air-guns in a marine seismic air-gun array are reflected from the water–air interface with negative polarity. Constructive interference of the sea-surface reflected acoustic waves "add up" and the absolute hydrostatic pressure drops close to zero in some regions which results in water vapor cavity growth and subsequent collapses (Landrø *et al.*, 2013; Landrø *et al.*, 2016). This phenomenon was numerically modeled based on air-gun modeling and bubble dynamic equations (Khodabandeloo *et al.*, 2017). Air-gun modeling (Ziolkowski *et al.*, 1982) is used to obtain notional source signatures of individual air-guns in the array. Using linear superposition of the pressure generated by individual air-guns, the temporal and spatial distribution of regions where the pressure is close to or below zero are determined. Afterward, Prosperetti bubble dynamics equations (Prosperetti and Lezzi, 1986) are used to estimate vapor cavity growth and collapse. The signal from collapse of several single vapor cavities within the cloud will also generate a low-frequency response (Khodabandeloo and Landrø, 2017a) in addition to the high frequencies. The strength and energy of the high-frequency ghost cavitation signal can actually be decreased while the energy in the useful frequency band increases. This depends on the configuration of the air-gun array (Khodabandeloo and Landrø, 2017b). Essentially, the ghost cavitation can be reduced by increasing the distance between the guns (Landrø *et al.*, 2016).

Liquids are prone to cavity formation and subsequent collapse where they experience pressure drop below the vapor pressure or partial pressure of dissolved gases (Mellen, 1954; Plesset, 1970). Acoustic cavitation is the term used for the vapor cavity induced due to the oscillating pressure when an acoustic wave propagates through a liquid (Frohly *et al.*, 2000; Apfel, 1984). In the case of pure water and in the absence of impurities or cavitation nuclei, there is a very high negative pressure (~ -26 MPa) required to rupture the water and form the cavity (Caupin and Herbert, 2006; Herbert *et al.*, 2006). Availability of cavity nuclei facilitates the cavity generation (Apfel, 1984; Brennen, 2013). This is shown in a Venturi nozzle experiment (Harrison, 1952) and an experiment by seeding cavities by electrolysis (Arakeri and Shanmuganathan, 1985) where it is observed that undissolved air bubbles with the size of typically 50 μm are excellent cavitation nuclei sites. It is estimated that microbubbles with the size between 18 and 350 μm are uniformly distributed down to 36 m depth in seawater at around 6 knots wind speed (Medwin, 1977).

Several experiments demonstrate that the collapse of cavity bubbles produce intense noise and damage (Kim *et al.*, 2014; Reisman and Brennen, 1996; Franc and Michel, 1988). In some cases, it is valid to neglect the influence of a bubble on the neighboring bubbles. Then the resulting acoustic signal generated by several bubbles is simply equal to the sum of the acoustic pressure generated by individual cavities (Harrison, 1952). In the case of coherent cavity collapses within the cloud, the noise and damage are greater than expected from a random cumulative effect of individual cavity collapses in the cloud (Wang and Brennen, 1999). It is shown (Arakeri and Shanmuganathan, 1985) that it is possible to predict the noise spectrum generated by a cavity cloud based on single cavity bubble dynamics if the bubble volume fraction or void fraction, α, is small (<0.1). For example, when the void fraction is small, the noise spectrum increases over the whole frequency range by increasing the number of cavities. However, if the number of cavities within a cloud increases beyond a certain limit, the generated noise will decrease [see Fig. 6 in Arakeri and Shanmuganathan (1985)]. This might be caused by the physical overlap of bubbles and distortion in the cavity bubble shapes near their maximum radii. It is shown that interaction of bubbles within the cloud can be neglected if the cloud interaction parameter [$\beta = \alpha_0(1-\alpha_0)A_0^2/R_0^2$] is less than one (Wang and Brennen, 1999; Brennen *et al.*, 1999). In this relation, α_0 is the initial void fraction, A_0 is the initial cloud radius (assuming spherical cloud) and R_0 is the initial bubble radius. For large values of the cloud interaction parameter, the bubble collapse pattern produces an inward acoustic wave and the corresponding shock wave is strengthened as a result of geometric focusing effects (Wang and Brennen, 1999).

In the current experiment, the ghost cavitation cloud is visualized from high-speed video recordings of a seismic air-gun array consisting of two subarrays. The video images show the generation of multiple cavities and these images strengthen the ghost cavitation hypothesis. Even though the time resolution is not excellent (8.3 ms between two frames), it is possible to observe the creation and disappearance of the ghost cavity cloud. The shape of the cloud at different stages is also possible to study by looking at several shots since they have slightly different time zero compared to each other. The air-gun firing system is not synchronized with the video recording. The ghost cavity cloud and the corresponding acoustic signal is simulated using the numerical modeling procedure proposed by Khodabandeloo *et al.* (2017). The cavity clouds observed by video recordings are compared to modeled cavity clouds. Finally, we compare the measured acoustic signal to the modeled signal.

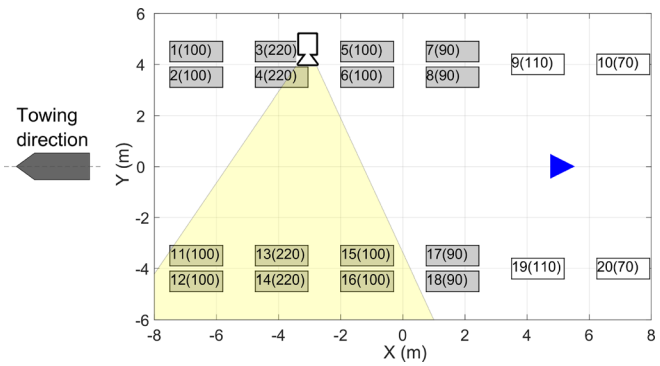

FIG. 1. (Color online) Air-gun array configuration used for the field experiment. There are 20 air-guns arranged in two subarrays and the air chamber volumes (in cubic inches) are shown next to the gun number within the parentheses. Single air-guns are shown by white rectangles and clustered air-guns by gray. The video camera is mounted on one of the subarrays (near guns 3 and 4) and its approximate view angle is shown as a yellow cone. The approximate location of the hydrophone is shown by the blue triangle.

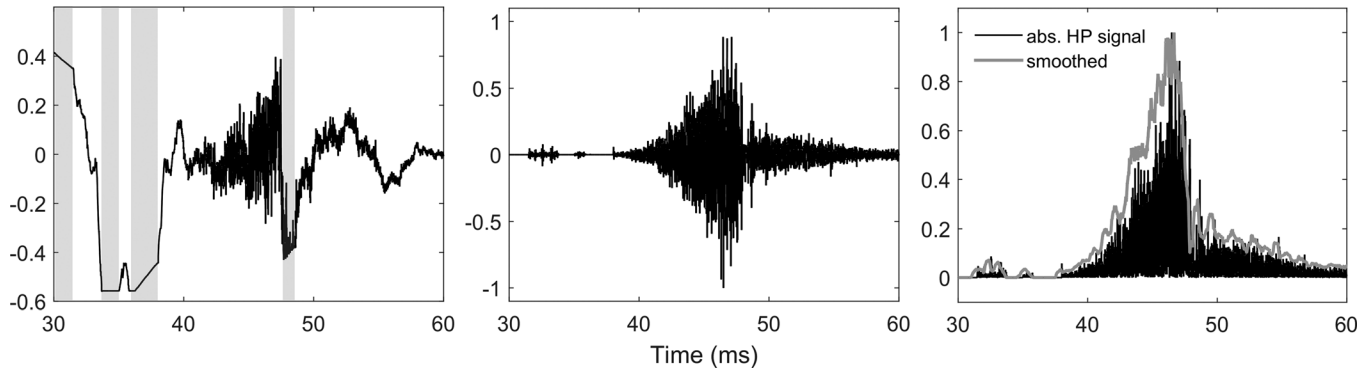

FIG. 2. Unfiltered measured signal for with a broadband hydrophone suspended around 17 m below the array (left). The saturated parts are indicated by gray vertical ribbons. Ten kilohertz high-pass filtered (middle). Absolute values of high-pass filtered data and its smoothed envelope (right). The source depth is 9 m and the subarray crossline separation distance is 8 m.

II. THE FIELD EXPERIMENT

The field experiment was conducted in 2011 offshore Congo in water depths between 1500 and 3000 m. The weather condition was good and the sea state was calm during the experiment. The source vessel was moving at a speed less than 2 knots (∼3.7 km/h). Field data that are used in this paper are from the source array configuration shown in Fig. 1. It consists of two subarrays where each one includes ten individual air guns. A high-speed underwater camera, with recording speed of 120 frames per second, was mounted on one of the subarrays with a view angle as shown in Fig. 1. A broadband hydrophone (bandwidth = 520 kHz) was suspended 17 m below the source array. There is an uncertainty related to the precise positioning of the hydrophone relative to the source array and most likely it deviates a few meters backward (off the vertical) due to towing effects. Top view of the approximate position of the hydrophone relative to the air-guns is shown in Fig. 1 (blue triangle).

The acoustic signals were recorded using a sampling interval of 0.0032 ms, and no gain was applied. The hydrophone sensitivity is 204 dB re 1 V/μPa. Measured signals beyond ±0.5 V were saturated (clipped). More details of the experimental setup can be found in Landrø *et al.* (2016).

A. High-frequency signal measurement

For a source depth of approximately 9 m and a subarray separation distance of approximately 8 m, a typical measured signal is shown in Fig. 2 (left). It is observed that some parts of the signal are saturated. For example, saturation occurs between ∼30 and 31 ms, ∼34 and 35 ms, ∼36 and 37.5 ms, and ∼47.5 and 48.5 ms. Fortunately, the ghost cavitation signal which is the focus of the experiment is not affected heavily by clipping. The reason is that the ghost cavitation signal arrives with some delay (∼6–20 ms) after the primary peak (Landrø *et al.*, 2011; Landrø *et al.*, 2013; Khodabandeloo *et al.*, 2017). For the signal shown in Fig. 2, the ghost cavitation signal is slightly affected by saturation effects for the time interval around 47.5–48.5 ms.

After applying a 10 kHz high-pass filter to the signals shown to left in Fig. 2, the result is shown in the middle picture of the same figure and the absolute values of the high-pass filtered signal and the smoothed envelope using a moving average filter are shown to the right. For four different shots, smoothed amplitudes of the 10 kHz high-pass filtered signals are plotted in Fig. 3. The curves indicate that the pattern and envelope of high-pass filtered ghost cavitation signals are highly repeatable. All the high-pass filtered signals share the same pattern: the energy is accumulated with a smaller rate in the beginning than at the end which causes a fast cessation of the signal at the end.

B. Field video recording

Air-guns 11 to 16 (Fig. 1) are present in the camera frame and four successive recorded frames are shown for four different shots in Fig. 4. Each row represents frames from one shot. The first image of each row is the first frame for each shot and shows the initial phase as the air escapes

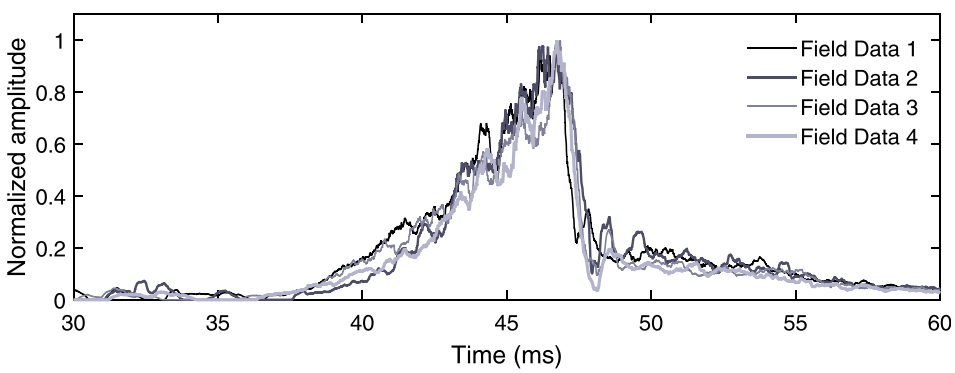

FIG. 3. (Color online) Smoothed absolute values of four 10 kHz high-pass filtered measured signals (shots).

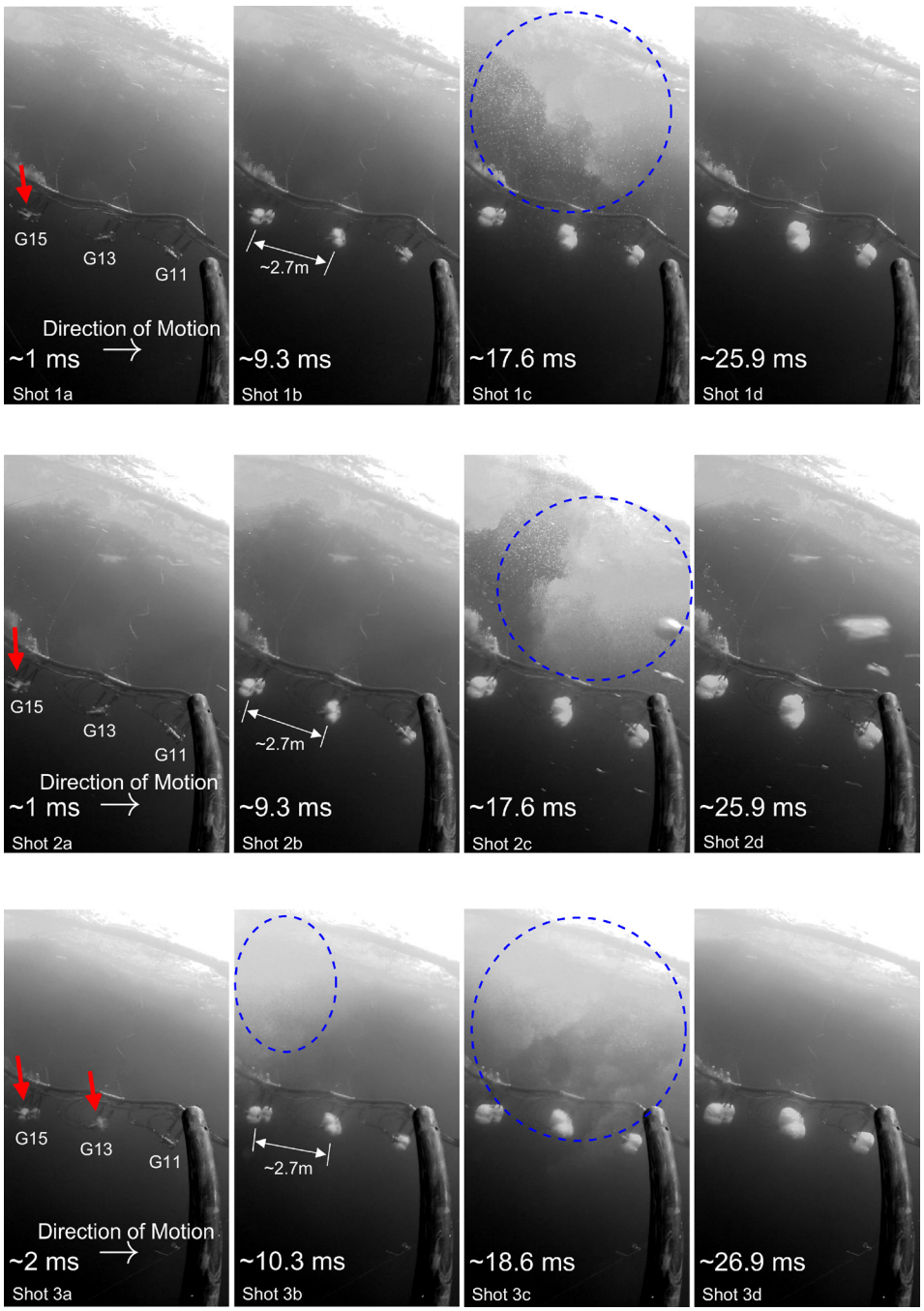

FIG. 4. (Color online) Video recording of part of one subarray using a high-speed camera (120 fps) mounted on the other subarray. Each row represents frames from one firing of the source array; a, b, c, and d refer to successive images from the same shot. Guns 11, 13, and 15 are in the camera frame and indicated by G11, G13, and G15. Red arrows indicate air escaping the air-gun(s) in the first frame of each shot. In shot 1a and shot 2a air is seen exiting gun 15 while no air is seen escaping gun 13 and 11. In shot 3a and shot 4a the air is only observed escaping gun 15 and 13 as indicated by the red arrows. The cavity cloud is observed in shot 1c, shot 2c, shot 3b, shot 3c, shot 4b, shot 4c, and indicated by blue dashed ellipses. If zero time is opening of air-gun ports, the associated time to the recorded frame time is assigned depending on amount of air exiting the gun(s) in the first frame: ∼1 ms for first and second rows (shot 1a and 2a) and ∼2 ms for third and fourth rows (shot 3a and 4a).

through the gun ports. Since the air-gun firing system is not synchronized with the video recording, the images in the first column do not correspond to the same stage after the guns are triggered. If time zero ($t = 0$) for each shot is the time when the earliest air-gun is fired (opening of air-gun ports), an approximate time can be estimated for the first frame. In the first frame of the first and second shots (rows) in Fig. 4 (denoted shot 1a and shot 2a, respectively) air is only observed escaping gun 15 (G15) as indicated by the red arrow. If time zero ($t = 0$) for the first source firing is when ports of gun 15 become open, based on the amount of air that has exited from gun 15 in shot 1a, the time instant corresponding to this frame (shot 1a) is estimated to be ∼1 ms. Using the same method for the other shots, a

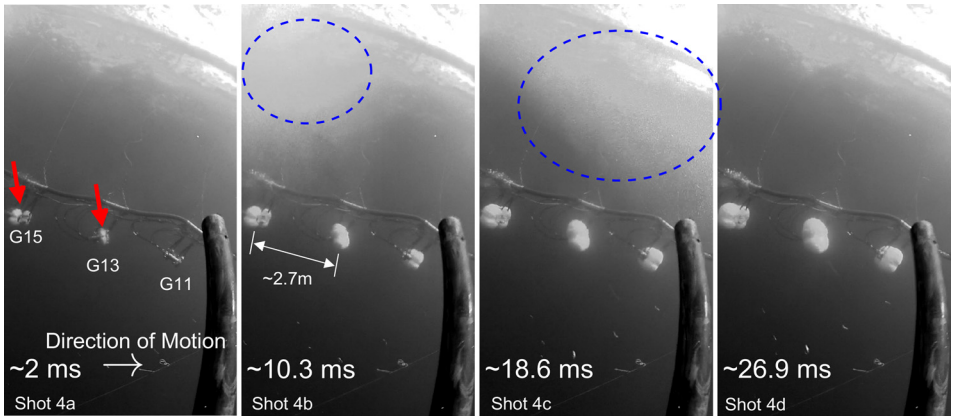

FIG. 4. (Color online) (*Continued*)

time instant for the first column is estimated, as shown in Fig. 4.

III. MODELING THE GHOST CAVITY CLOUD

The simulation method is summarized in the Appendix and for more details of the simulation technique, we refer to Khodabandeloo *et al.* (2017). Using the source array shown in Fig. 1, pressure variations at different locations around the air-gun array are estimated by adding the pressure from each air-gun to the hydrostatic pressure of the corresponding location. The response of a stable free microbubble with an equilibrium radius of 20 μm to the estimated pressure variations is estimated by Eq. (A1) in the Appendix. In the simulation, due to the observed delays between air-gun firings in the first image of each row in Fig. 4, all the air-guns are not fired simultaneously and some of them are fired with some minor delays. We have assumed the guns in each cluster (for example, guns 15 and 16 form one cluster) are fired simultaneously. Furthermore, we assume that the two subarrays have same performance which means for example gun 5 and 6 are activated simultaneously with gun 15 and 16. It is the same for guns 3, 4, 13, and 14. Guns 1, 2, 11, and 12 are fired simultaneously as well. The remaining guns which are not in the images, that is guns 17 to 20 and guns 7 to 10 are fired simultaneously with gun 15.

For an air-gun, the peak pressure occurs approximately at the time when the air escapes through the ports. For simplicity, we choose the time when the first air is visible at the port opening as time zero. Selecting the time when the modeled pressure of earliest gun(s) reaches its peak value as zero time (t = 0) in the simulation, ensures having roughly the same time reference between the simulated and the photographed cavity cloud.

Based on the amount of air released from the guns in the first image in each row in Fig. 4, we estimated a time delay of 2.5 ms for guns 1, 2, 11, and 12 and a time delay of 1.5 ms for guns 3,4, 13, and 14.

The temporal and spatial distributions of minimum pressures are obtained from air-gun modeling and are shown in Fig. 5. The computational domain uses a three-dimensional grid with a spatial resolution of 0.2 m and it is assumed that

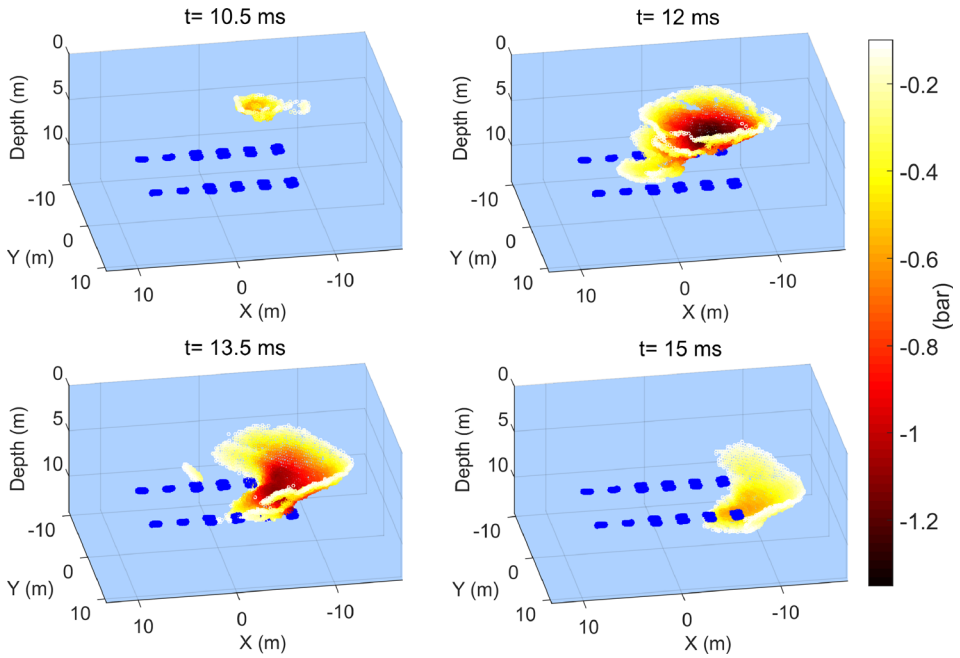

FIG. 5. (Color online) Simulated minimum pressure distributions for four time instants (t = 10.5, 12, 13.5, 15 ms) for the case of firing some guns delayed with respect to the others in the array.

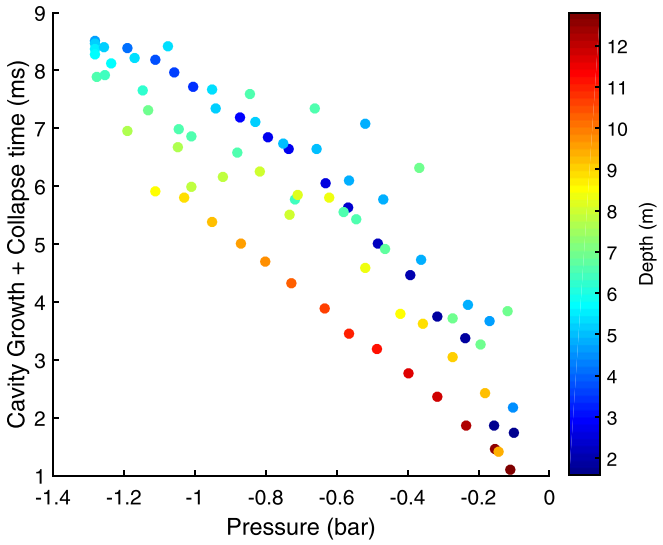

FIG. 6. (Color online) Cavity lifetimes (growth + collapse times) at different locations around the array as a function of the minimum pressure of external pressure that each cavity had been exposed to for the case of firing some air-guns with the delay in the array. Bubble dynamic Eq. (A1) is solved for each cavity to estimate its lifetime.

a cavity is formed if the pressure drops below a certain level (−0.1 bar) at that grid location. The temporal sampling interval for the simulations is 0.1 ms.

Cavity lifetimes (growth + collapse times) at different locations are estimated using Eq. (A1), given in the Appendix, are shown as a function of minimum external pressure and depth in Fig. 6.

The time when the pressure reaches its minimum and fulfills the requirement (<−0.1 bar) for cavity creation is considered as the initiation time for that specific cavity. Having the initiation time (Fig. 5) and the lifetime of each cavity (Fig. 6), we know the timing when each cavity appears in the cloud. Modeled cavity clouds for six time instants are shown in Fig. 7.

The modeling predicts that a cavity cloud is formed above the source array. Then it moves slightly downwards and to the right (Fig. 7). The cloud shape and pattern resemble the photographed cavity cloud. Simulation results indicate that the cavity cloud is present for around 10 ms, which means if it is video-recorded every 8.3 ms, it will appear at most in two frames which is in agreement with the video recordings shown in Fig. 4.

If all air-guns are fired simultaneously, the modeled cavity cloud will be somewhat different, as shown in Fig. 8.

The cloud is initiated somewhere in the middle top of the array and then moves to both sides and extends downwards. Figures 6 and 5 will also be different for the case when all guns are fired at the same time.

IV. COMPARISON OF NUMERICAL MODELING AND FIELD MEASUREMENTS

The simulated cavity cloud assuming relative delays in air-gun firing times (Fig. 7) better resembles the photographed

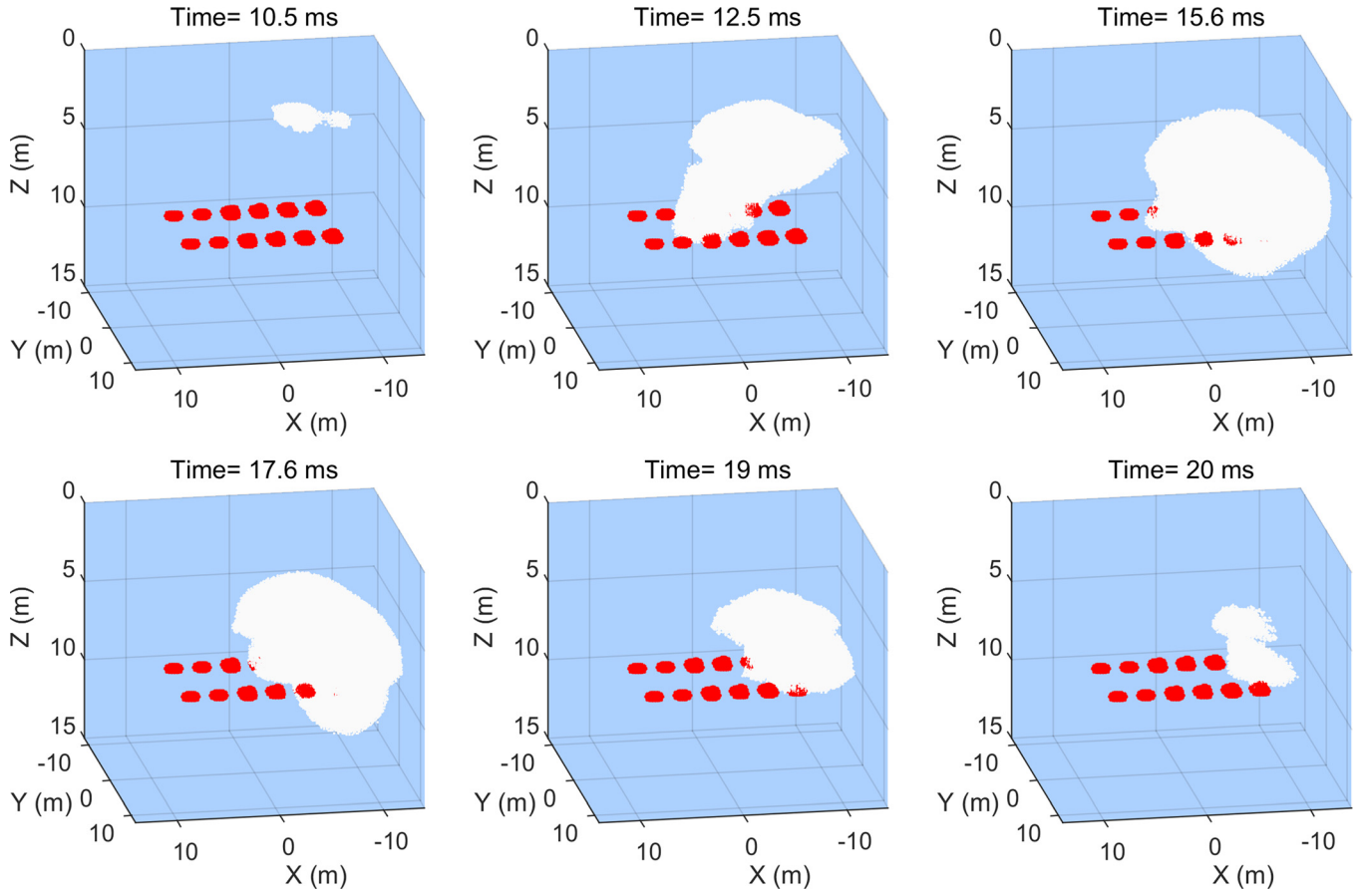

FIG. 7. (Color online) Simulated cavity cloud for the case where some air-guns are fired with some delay in the array.

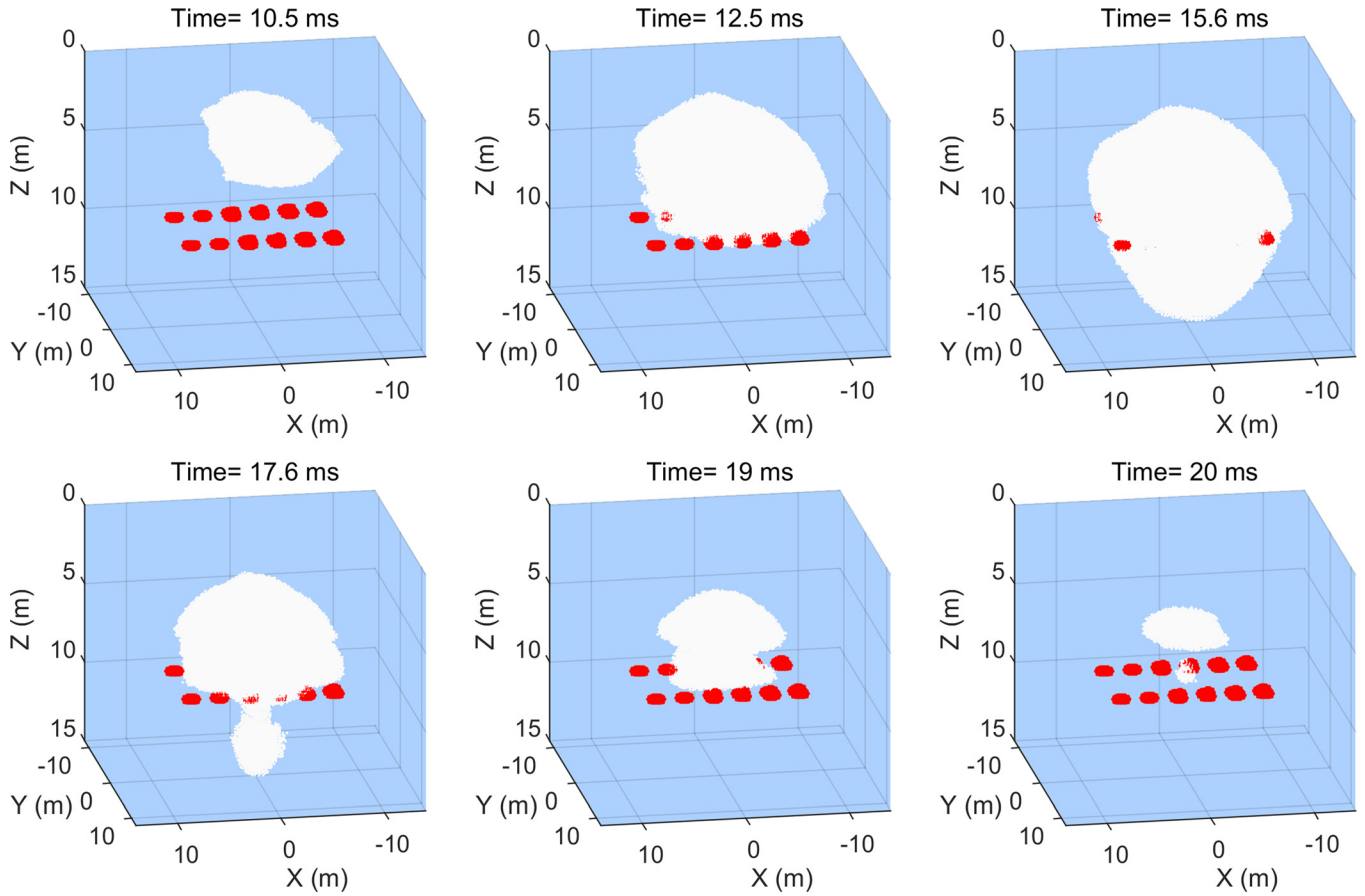

FIG. 8. (Color online) Simulated cavity cloud for the case where all air-guns in the array are fired simultaneously.

cavity cloud than assuming that all guns are fired simultaneously (Fig. 8). To have a closer look at the modeled and photographed cavity cloud, the image from the video recording and the corresponding simulated cavity cloud are shown in Fig. 9 for a time instant of 17.6 ms. To compare with the photographed cavity cloud, a cut section of the modeled cloud (Fig. 9; right) is shown to include only one subarray in the image.

The camera frame is approximately shown by the green transparent plane in the modeled cloud shown in Fig. 9 (right). In our modeling, at each grid point a cavity grows—and subsequently collapses—provided that a minimum pressure threshold is fulfilled at that grid point. Hence, the grid resolution determines the initial number of cavities in the modeling. The actual number of cavities can be determined by calibrating the model such that the amplitude, energy, or

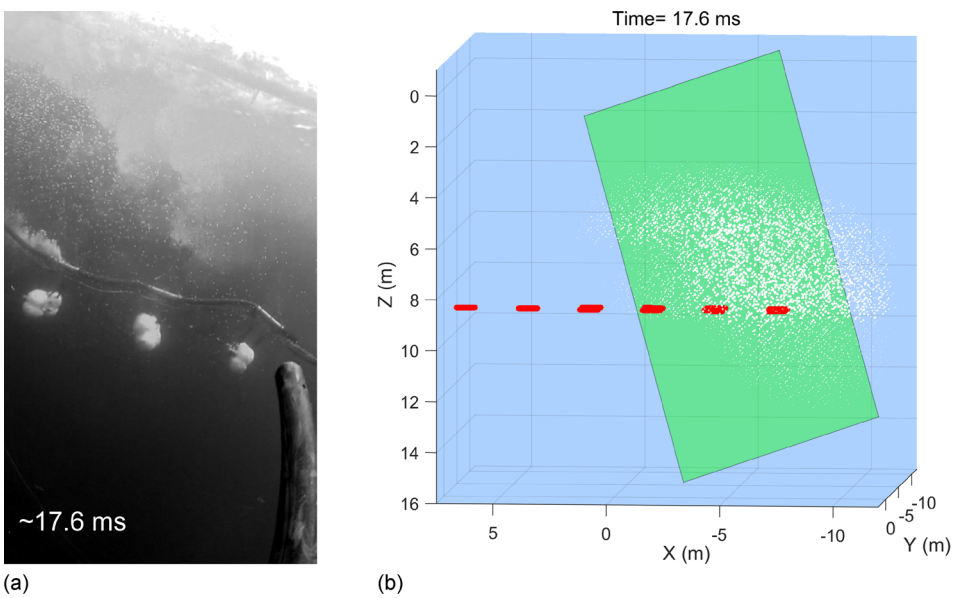

FIG. 9. (Color online) Comparison of the cavity cloud observed from video recording and the corresponding numerical modeling. In the modeled cloud, the corresponding frame of the camera is approximately shown by the green plane.

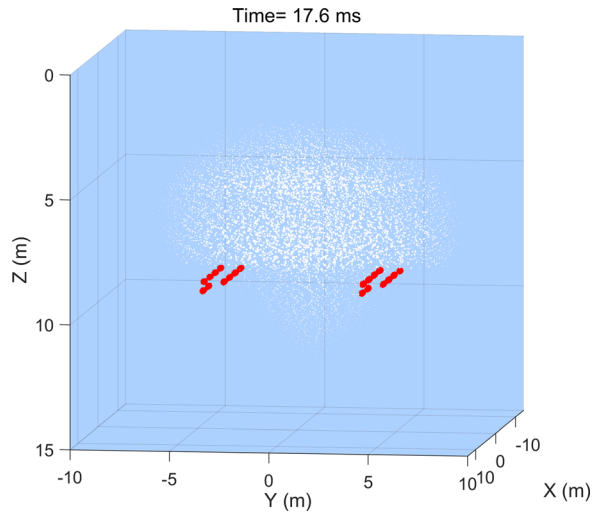

FIG. 10. (Color online) Front view of the modeled cavity cloud at 17.6 ms. The number of plotted cavities is reduced by a factor of 14 compared to the number of cavities based on selected grid resolution.

frequency content of the modeled ghost cavitation signals matches the measurements. However, the calibration highly relies on the calculated acoustic pressure signatures from collapses of individual vapor cavities since there is a tradeoff between the strength of each cavitation signal and the number of cavities. The calculated acoustic pressure signature from collapse of individual vapor cavity seems to have a very high peak compared to the experimental results of single cavity collapses (Versluis *et al.*, 2000). One cause might be that diffusion of dissolved gases (Plesset, 1970; Prosperetti, 2017) is ignored in the bubble dynamic equation. Diffusion adds some permanent gas to the cavity and cushions the collapse (Neppiras, 1984). The other reason might be the interaction between the growing cavity and the pressure fields from other cavity collapses. For a different air-gun array but the same grid resolution as we used here, Khodabandeloo and Landrø (2017a) calibrated the model (on a trial and error basis) such that both the amplitude of high-frequency modeled signal and its associated low-frequency part matched the measurements. In that paper we artificially reduced the peak pressure of individual cavity collapse signatures and determined a single scaling factor equal to 0.07 (≈1/14) that gave a good match for both the amplitude of the modeled high frequency signal and its associated low-frequency part. This means that the assumed number of cavities should be reduced by factor of 14. Therefore, the number of cavities shown in the modeled cloud in Fig. 9 is reduced compared to the corresponding time (17.6 ms) in Fig. 7 by a factor of 14. As seen in the front view of the modeled cavity cloud in Fig. 10, the majority of the cloud is formed midway between the two arrays.

It should be noted that we do not claim that our model is calibrated in a systematic manner, nor is it the scope of this paper. For the current modeling results, we have applied a calibration factor which was obtained for the same modeling scheme using the same grid resolution but based on another field experiment with a different air-gun array configuration (three subarrays instead of two). Applying that calibration factor to the current model, the agreement between the modeled and the photographed cloud was improved. To calibrate the model in a more systematic way, dedicated experiments are required to estimate cavity sizes, the pressure signatures from single cavity collapse, and non-clipped broadband recorded signals at different locations are needed for more than one or two array configurations.

The 10 kHz high-pass filtered measured signal is shown in Fig. 11 (top). Modeled ghost cavitation acoustic signals are shown in the second and third rows of Fig. 11. Simulation 1 is the 10 kHz high-pass filtered modeled ghost cavitation signal without including reflection of acoustic pressure of cavities from the sea surface. In simulation 2, reflection of ghost cavities from the sea surface assuming a reflection coefficient of −0.4 is included. For rough sea surface and high frequencies it

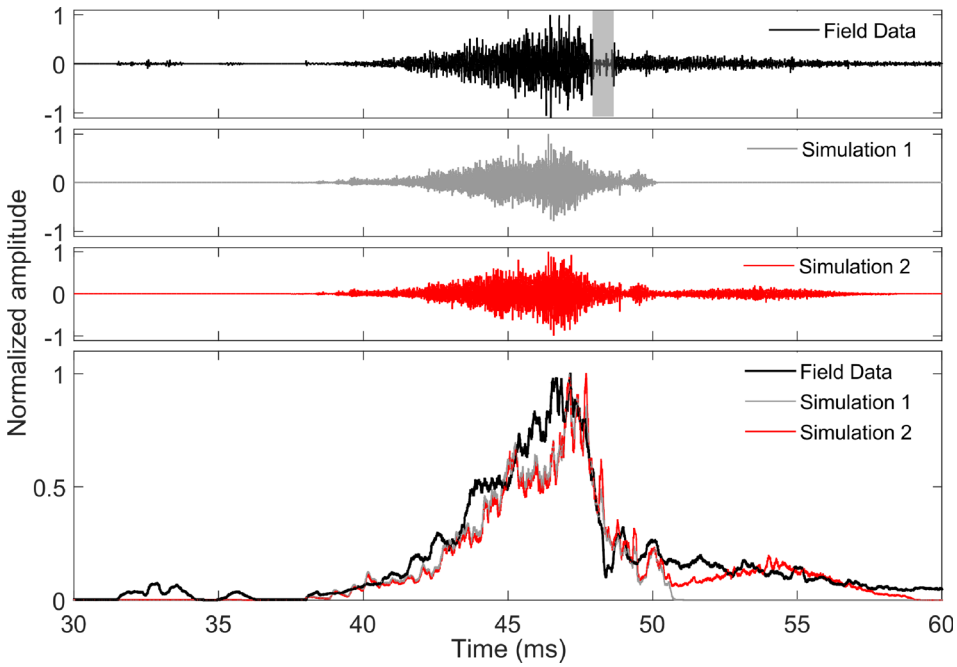

FIG. 11. (Color online) 10 kHz high-pass filtered ghost cavitation signal from field measurement (top), simulation 1 (second image from top) where the reflection of cavity signatures from sea surface is ignored. In simulation 2 (third from top) reflection of cavity signatures from the sea surface with reflection coefficient = −0.4 is included. In the top panel, the gray vertical ribbon indicates part of the signal that is clipped and cannot be compared directly with the modeled signal. Envelopes of absolute values are smoothed using a moving average method (bottom). All curves are normalized to one.

is reasonable to assume that the reflection coefficient is reduced significantly (Clay and Medwin, 1977, Landrø *et al.*, 2013). Both synthetic and field data show a gradual amplitude increase followed by a rapid decrease. When including the ghost reflections of the ghost cavity signals from the sea surface, the simulated signal predicts the observed long tail after the rapid decrease in the field data (Fig. 11).

The envelope of absolute values of the field data, simulation 1, and simulation 2 are smoothed using a moving average window and plotted in Fig. 11 (bottom). It is seen that there is a good agreement between modeled and measured curves regarding their time duration and shape of envelopes.

V. DISCUSSION

In the modeled cavity cloud, we have assumed one stable microbubble with radius 20 μm at each grid point in the computation domain with cell sizes of $0.2\,\mathrm{m} \times 0.2\,\mathrm{m} \times 0.2\,\mathrm{m}$. The void fraction, $\alpha_{0,}$ in our example is $0.07 \times (4/3)\pi R_0^3/0.2^3 = 2.9 \times 10^{-13}$, where 0.07 is the scaling factor that we discussed in Sec. IV. By void fraction we refer to those stable microbubbles within the sea water acting as cavity nucleation site. Assuming the equivalent spherical cloud radius equal to 5 m, then the cloud interaction parameter is estimated by $\beta = \alpha_0(1-\alpha_0)A_0^2/R_0^2 = 0.018$. Considering the values of the void fraction and cloud interaction parameter, the bubble–bubble interaction within the cloud can be neglected (Wang and Brennen, 1999; Brennen *et al.*, 1999; Arakeri and Shanmuganathan, 1985). For an air-gun array the asynchronicity between air-guns is normally less than 1 ms. Weighting the assigned time delay of each air-gun by its air-chamber volume, the average delay is 0.97 ms in this experiment. Even though the allocated time delays for the air-guns in our modeling seem a bit larger than the expected time delays in an air-gun array, they improve the similarity between the modeled and imaged cavity cloud. Moreover, we do not have access to the detailed firing time delays in the current experiment where the video recordings indicate that actual firing time delays might be slightly higher compared to normal operations.

It should be noted that the shapes of the cloud pattern observed from the video recordings vary from shot to shot which is probably caused by slightly different firing time delays for each shot. However, the recorded high-frequency acoustic signal is highly repeatable. Even though cavity collapse interaction and possible non-linear phenomena, as well as effects of cavitation cloud on acoustic propagation such as reduction in sound speed and increase in attenuation, are ignored, there is a good agreement between the modeled and field data in terms of the time duration and signal envelope shape. However, the model needs calibration such that the amplitude, energy, and frequency contents of modeled ghost cavitation signals match the measured. To do so, it would be necessary to record the non-saturated (non-clipped) acoustic signature at several locations for more than one source array.

VI. CONCLUSION

The ghost cavity cloud generated by an air-gun array is observed using a high-speed (120 frames per second) video camera. The photos of the ghost cavity cloud support the hypothesis of source ghost cavitation. From the images it is clearly observed that multiples of cavities appear for a short time interval (10 ms) after the guns are fired. Synthetic modeling predicts an onset time as well as the time duration of the cavitation signal that fits the field observations. Furthermore, the modeled shape and position of the cavity cloud resemble those of the video recordings. There is a good agreement between the field-recorded high-frequency acoustic signals and those from the modeling with respect to their envelope shape and time duration. To calibrate the model such that the amplitude, energy, and frequency content of the simulated signal match the measured one, it is required to have non-saturated broadband field-recorded signals from two or more different air-gun array configurations.

For future field experiments to better capture the ghost cavitation phenomenon, it is suggested to perform the video recording with higher speed (>480 fps) and use two cameras; one in front of the array and one at the side.

ACKNOWLEDGMENT

We thank Statoil and CGG for permission to present this work, and for funding the experiments presented in this paper. The authors would like to thank Lasse Amundsen and Risto Siliqi for reading the manuscript and constructive comments. This research is funded by Research Center for Arctic Petroleum Exploration (ARCEx) partners, and the Research Council of Norway (Grant No. 228107). M.L. acknowledges the Norwegian Research Council for financial support to the ROSE consortium at NTNU. The reviewers are acknowledged for providing detailed comments and invaluable suggestions to strengthen the quality of the manuscript.

APPENDIX: GHOST CAVITATION MODELING

An air-gun array consists of several individual air-guns with different air chamber volumes. The array used for this study consists of 20 air-guns arranged in two subarrays as shown in Fig. 1. Hydrostatic pressure can drop below a certain threshold at some locations around the array as a result of the reflected acoustic pressure of individual air-gun from the sea-surface. The pressure at two different locations around the array are shown by dashed curves in Fig. 12. It is seen that the hydrostatic pressure becomes negative based on linear theory from the superposition of pressures from individual air-guns in the array. From the initial part of the pressure curves, it is seen that the one shown in the right graph belongs to a deeper location since it has larges hydrostatic pressure. It is possible to estimate the response of a tiny stable bubble subjected to the external pressure, P, in the following bubble dynamics equation (Prosperetti and Lezzi, 1986):

$$\left(1-\frac{1}{c}\frac{dR}{dt}\right)R\frac{d^2R}{dt^2}+\frac{4\mu}{\rho c}\frac{d^2R}{dt^2} = -\frac{3}{2}\left(1-\frac{1}{3c}\frac{dR}{dt}\right)\left(\frac{dR}{dt}\right)^2-\frac{1}{\rho R}\left[2\sigma+4\mu\frac{dR}{dt}\right] +\frac{1}{\rho}\left(1+\frac{1}{c}\frac{dR}{dt}\right)[P_i(t)-P]+\frac{R}{\rho c}\frac{dP_i(t)}{dt}. \quad \text{(A1)}$$

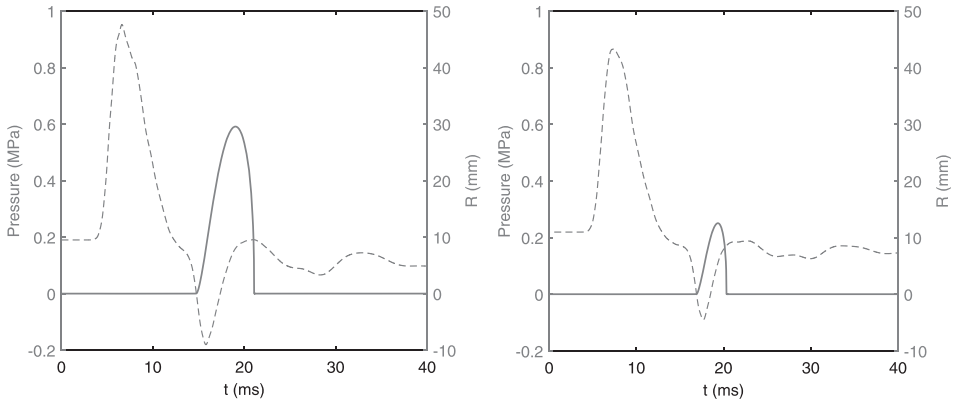

FIG. 12. Response of a stable microbubble (solid curve) to pressure variations (dashed curve) at two different locations estimated from bubble dynamic equation given in Eq. (A1). Left picture corresponds to a location with smaller depth compared to the right picture as seen from its smaller initial hydrostatic pressure.

In the above equation, $R(t)$ denotes the time-dependent cavity radius, $c = 1500\,\text{m/s}$ is the sound speed of undisturbed water, $\sigma = 0.074\,\text{N/m}$ is the water surface tension (Nayar *et al.*, 2014), $\rho = 1000\,\text{kg/m}^3$ is the density of water, and $\mu = 0.001\ \text{Ns/m}^2$ is the dynamic viscosity of water. The pressure inside the cavity is shown by $P_i(t)$ and is modeled by Van der Waals equation. Substituting two pressure time curves given in Fig. 12 as external pressure in Eq. (A1) the response of a bubble with initial size of 20 μm are estimated by solving the differential equation by means of the Runge-Kutta method of order 5 ("ode45" algorithm in MATLAB) and plotted as solid curves in the same figure. There are microbubbles with the size between 18 and 350 μm uniformly distributed up to 36 m depth in the sea at wind speed of around 6 knots (Medwin, 1977).

Collapses of individual cavities generate acoustic pressure and its signature in the far-field is estimated by (Brennen, 2013; Leighton, 2012)

$$p(t) = \frac{\rho R}{r}\left(2\dot{R}^2 + R\ddot{R}\right). \tag{A2}$$

In the above equation, the superposed dot indicates a time derivative. Acoustic pressure signature of individual cavities obtained by Eq. (A2) is propagated from where it is generated to the receiver location:

$$u_i(t,r) = \frac{1}{\sqrt{2\pi}}\int_{-\infty}^{+\infty}\left(S_i(f)\cdot e^{-\gamma(f)r_i}\cdot e^{-j2\pi f\tau_i}\cdot\frac{e^{-j(2\pi f/c)r_i}}{r_i}\right)e^{j2\pi tf}\,df. \tag{A3}$$

For the ith cavity, the distance between cavity source and its measured location is denoted by r_i, and τ_i shows its formation time. In the propagation, geometrical spreading and absorptions are included. $S_i(f)$ is the frequency domain representation of the time signal from the collapse of the ith cavity. γ stands for absorption (Np/m) and is calculated from the equation given by Francois and Garrison (1982). Adding the pressure signature of individual cavities given in Eq. (A3), it is possible to simulate the cavitation signal from the cloud of cavities. Detailed modeling steps of the ghost cavity cloud are given in Khodabandeloo *et al.* (2017).

Apfel, R. E. (**1984**). "Acoustic cavitation inception," Ultrasonics **22**(4), 167–173.

Arakeri, V. H., and Shanmuganathan, V. (**1985**). "On the evidence for the effect of bubble interference on cavitation noise," J. Fluid Mech. **159**, 131–150.

Banda, N., and Blondel, P. (**2016**). "Identifying mid-water targets using the higher frequencies emitted by seismic sources of opportunity," *in Oceans'16*, MTS/IEEE, Monterey, pp. 1–7.

Barger, J. E., and Hamblen, W. R. (**1980**). "The air gun impulsive underwater transducer," J. Acoust. Soc. Am. **68**(4), 1038–1045.

Brennen, C. E. (**2013**). *Cavitation and Bubble Dynamics* (Cambridge University Press, London).

Brennen, C., Colonius, T., Wang, Y. C., and Preston, A. (**1999**). "Cloud cavitation phenomena," in *Twenty-Second Symposium on Naval Hydrodynamics*, The National Academy of Sciences, pp. 239–253.

Caldwell, J., and Dragoset, W. (**2000**). "A brief overview of seismic air-gun arrays," Leading Edge **19**(8), 898–902.

Caupin, F., and Herbert, E. (**2006**). "Cavitation in water: A review," C. R. Phys. **7**(9), 1000–1017.

Chelminski, S. (**2015**). "Device for marine seismic explorations for deposits," U.S. patent 8,971,152 B2 (February 23, 2014).

Clay, C. S., and Medwin, H. (**1977**). *Acoustical Oceanography: Principles and Applications* (Wiley, New York).

Coste, E., Gerez, D., Groenaas, H., Hopperstad, J. F., Larsen, O. P., Laws, R., Norton, J., Padula, M., and Wolfstirn, M. (**2014**). "Attenuated high frequency emission from a new design of air-gun," in *84th Annual International Meeting*, SEG, Expanded Abstracts, pp. 132–137.

Dragoset, B. (**2000**). "Introduction to air guns and air-gun arrays," Leading Edge **19**(8), 892–897.

Duren, R. E. (**1988**). "A theory for marine source arrays," Geophysics **53**(5), 650–658.

Franc, J. P., and Michel, J. M. (**1988**). "Unsteady attached cavitation on an oscillating hydrofoil," J. Fluid Mech. **193**, 171–189.

Francois, R. E., and Garrison, G. R. (**1982**). "Sound absorption based on ocean measurements. Part II: Boric acid contribution and equation for total absorption," J. Acoust. Soc. Am. **72**(6), 1879–1890.

Frohly, J., Labouret, S., Bruneel, C., Looten-Baquet, I., and Torguet, R. (**2000**). "Ultrasonic cavitation monitoring by acoustic noise power measurement," J. Acoust. Soc. Am. **108**(5), 2012–2020.

Gerez, D., Groenaas, H., Larsen, O. P., Wolfstirn, M., and Padula, M. (**2015**). "Controlling air-gun output to optimize seismic content while reducing unnecessary high-frequency emissions," in *2015 Society of Exploration Geophysicists Annual Meeting*.

Goold, J. C., and Fish, P. J. (**1998**). "Broadband spectra of seismic survey air-gun emissions, with reference to dolphin auditory thresholds," J. Acoust. Soc. Am. **103**(4), 2177–2184.

Groenaas, H., Gerez, D., Larsen, O. P., and Padula, M. (**2016**). "On the anatomy of the air-gun signature," in *SEG Technical Program Expanded Abstracts*, Society of Exploration Geophysicists, pp. 46–50.

Guan, S., Vignola, J., Judge, J., and Turo, D. (**2015**). "Airgun inter-pulse noise field during a seismic survey in an Arctic ultra-shallow marine environment," J. Acoust. Soc. Am. **138**(6), 3447–3457.

Harrison, M. (**1952**). "An experimental study of single bubble cavitation noise," J. Acoust. Soc. Am. **24**(6), 776–782.

Herbert, E., Balibar, S., and Caupin, F. (**2006**). "Cavitation pressure in water," Phys. Rev. E **74**(4), 041603.

Ketten, D. R. (**2004**). "Marine mammal auditory systems: A summary of audiometric and anatomical data and implications for underwater acoustic impacts," Polarforschung **72**(2–3), 79–92.

Khodabandeloo, B., and Landrø, M. (**2017a**). "Effects of Ghost cavitation cloud on near-field hydrophones measurements in the seismic air gun arrays," in *79th EAGE Conference and Exhibition*.
Khodabandeloo, B., and Landrø, M. (**2017b**). "High frequency ghost cavitation-a comparison of two seismic air-gun arrays using numerical modeling," Energy Procedia **125**, 153–160.
Khodabandeloo, B., Landrø, M., and Hanssen, A. (**2017**). "Acoustic generation of underwater cavities—Comparing modeled and measured acoustic signals generated by seismic air gun arrays," J. Acoust. Soc. Am. **141**(4), 2661–2672.
Kim, K. H., Chahine, G., Franc, J. P., and Karimi, A., eds. (**2014**). *Advanced Experimental and Numerical Techniques for Cavitation Erosion Prediction* (Springer, Dordrecht), Vol. 106.
King, J. R. C. (**2015**). "Air-gun bubble-ghost interactions," Geophysics **80**(6), T223–T234.
King, J. R. C., Ziolkowski, A. M., and Ruffert, M. (**2015**). "Boundary conditions for simulations of oscillating bubbles using the non-linear acoustic approximation," J. Comput. Phys. **284**, 273–290.
Landrø, M., Amundsen, L., and Barker, D. (**2011**). "High-frequency signals from air-gun arrays," Geophysics **76**(4), Q19–Q27.
Landrø, M., Amundsen, L., and Langhammer J. (**2013**). "Repeatability issues of high-frequency signals emitted by air-gun arrays," Geophysics **78**, P19–P27.
Landrø, M., Hansteen, F., and Amundsen, L. (**2017**). "Detecting gas leakage using high-frequency signals generated by air-gun arrays," Geophysics **82**(2) A7–A12.
Landrø, M., Ni, Y., and Amundsen, L. (**2016**). "Reducing high-frequency ghost cavitation signals from marine air-gun arrays," Geophysics **81**(3), P33–P46.
Leighton, T. (**2012**). *The Acoustic Bubble* (Academic, New York).
Medwin, H. (**1977**). "*In situ* acoustic measurements of microbubbles at sea," J. Geophys. Res. **82**(6), 971–976, https://doi.org/10.1029/JC082i006p00971.
Mellen, R. H. (**1954**). "Ultrasonic spectrum of cavitation noise in water," J. Acoust. Soc. Am. **26**(3), 356–360.
Nayar, K. G., Panchanathan, D., and McKinley, G. H. (**2014**). "Surface tension of seawater," J. Phys. Chem. Ref. Data **43**(4), 043103.
Neppiras, E. A. (**1984**). "Acoustic cavitation series: Part one: Acoustic cavitation: An introduction," Ultrasonics **22**(1), 25–28.
Plesset, M. S. (**1970**). "Effect of dissolved gases on cavitation in liquids (No. 85-55)," Pasadena Division of Engineering and Applied Science, California Institute of Technology.
Prosperetti, A. (**2017**). "Vapor bubbles," Ann. Rev. Fluid Mech. **49**, 221–248.
Prosperetti, A., and Lezzi, A. (**1986**). "Bubble dynamics in a compressible liquid. Part 1. First-order theory," J. Fluid Mech. **168**, 457–478.
Reisman, G. E., and Brennen, C. E. (**1996**). "Pressure pulses generated by cloud cavitation," in *ASME Symposium on Cavitation and Gas-Liquid Flows in Fluid Machinery and Devices*, San Diego, CA, FED, Vol. 236, pp. 319–328.
Ronen, S., and Chelminski, S. (**2017**). "Tuned pulse source—A new low frequency seismic source," in *SEG Technical Program Expanded Abstracts*, Society of Exploration Geophysicists, pp. 6085–6088.
Tashmukhambetov, A. M., Ioup, G. E., Ioup, J. W., Sidorovskaia, N. A., and Newcomb, J. J. (**2008**). "Three-dimensional seismic array characterization study: Experiment and modeling," J. Acoust. Soc. Am. **123**, 4094–4108.
Versluis, M., Schmitz, B., von der Heydt, A., and Lohse, D. (**2000**). "How snapping shrimp snap: Through cavitating bubbles," Science **289**(5487), 2114–2117.
Wang, Y. C., and Brennen, C. E. (**1999**). "Numerical computation of shock waves in a spherical cloud of cavitation bubbles," ASME J. Fluids Eng. **121**(4), 872–880.
Watson, L., Dunham, E., and Ronen, S. (**2016**). "Numerical modeling of seismic airguns and low-pressure sources," in *SEG Technical Program Expanded Abstracts*, Society of Exploration Geophysicists, pp. 219–224.
Ziolkowski, A., Parkes, G., Hatton, L., and Haugland, T. (**1982**). "The signature of an air gun array: Computation from near-field measurements including interactions," Geophysics **47**(10), 1413–1421.